Journal of Molecular Structure 1353 (2026) 144655

Contents lists available at ScienceDirect

Journal of Molecular Structure

journal homepage: www.elsevier.com/locate/molstr

Pyridine-linked 1,3,4-oxadiazoles decorated with secondary amines as α-amylase inhibitors: Synthesis, crystal structure, enzyme kinetics and computational studies

Chandan Mallikarjuna [a], Udaya Kumar A. H [b,c], Karthik Kumara [d,e], Rekha N Dharmappa [f], Dinesh Kumar G [g], Neratur Krishnappagowda Lokanath [b], Kariyappa Ajay Kumar [a,*]

[a] Department of Chemistry, Yuvaraja College, University of Mysore, Mysuru, 570 005, Karnataka, India
[b] Department of Studies in Physics, University of Mysore, Manasagangotri, Mysuru 570006, Karnataka, India
[c] Department of Physics, Seshadripuram Institute of Technology, Mysuru, 571 311, Karnataka, India
[d] Department of Physics, B.M.S. College of Engineering, Bengaluru, 560 019, Karnataka, India
[e] B S Narayan Centre for Nano-materials and Displays, B. M. S. College of Engineering, Bengaluru, 560 019, Karnataka, India
[f] Postgraduate Department of Biotechnology, JSS College of Arts, Commerce, Ooty Road, Mysuru, 570 025, Karnataka, India
[g] Govt. First Grade College, Hosaduga, 577 527, Karnataka, India

ARTICLE INFO

Keywords:
Pyridine-linked 1,3,4-oxadiazole
Secondary amine decoration
α-Amylase inhibition
Enzyme kinetics
X-ray diffraction
DFT calculations

ABSTRACT

A new series of pyridine-linked 1,3,4-oxadiazole derivatives **(5a–5j)** incorporating different secondary amines were synthesized in good yields (80–92 %) and their structures confirmed by ^{1}H and ^{13}C NMR spectroscopy and mass spectrometry. Biological screening revealed that compound **5c** displayed the strongest α-amylase inhibition with an IC_{50} of 106.1 ± 1.21 μM, compared with the standard drug acarbose (35.8 ± 1.25 μM). Enzyme kinetic studies (Lineweaver-Burk analysis) demonstrated that **5c** acts through a non-competitive inhibition mechanism, increasing Km from 27.36 μM (control) to 135.77 μM, while reducing Vmax from 1.55 μM min^{-1} to 0.135 μM min^{-1}. The structure of **5c** was further validated by single-crystal X-ray diffraction, and Hirshfeld surface analysis highlighted key intermolecular interactions, predominantly H···H (45.1 %), H···N (18.4 %), and H···C (12.6 %). Density Functional Theory calculations at the B3LYP/6–311+G(d,p) level reproduced the crystal geometry and indicated a HOMO-LUMO gap of 3.898 eV, consistent with moderate electronic reactivity. Molecular docking revealed that Compound **5c** showed strong α-amylase binding with docking energies of -7.7 to -8.0 kcal mol^{-1} outperforming reference inhibitor acarbose and indicating superior inhibitory efficacy. ADME profiling supported the drug-like nature of **5c** (MW = 323.35 g·mol^{-1}, logP = 0.42, TPSA = 84.07 $Å^2$, zero Lipinski violations), suggesting good oral bioavailability. Collectively, these experimental and computational findings identify **5c** as a promising lead scaffold for the design of new antidiabetic agents.

1. Introduction

Diabetes mellitus is a chronic metabolic disorder with a rapidly rising global prevalence. Type 2 diabetes (T2D) accounts for 90–95 % of cases and contributes significantly to morbidity and mortality [1]. According to the IDF Diabetes Atlas 2025, 11.1 % of adults aged 20–79 years (≈1 in 9) are affected, with over 40 % undiagnosed; by 2050, cases may reach 853 million worldwide (www.idf.org, accessed 04 September 2025). Diabetes also heightens cardiovascular, renal, and infectious risks, as seen during the COVID-19 pandemic [2]. Postprandial hyperglycemia, an early T2D feature, can be managed by inhibiting α-amylase (EC 3.2.1.1)-a salivary and pancreatic enzyme that breaks down α-linked polysaccharides into maltose-followed by α-glucosidase cleavage of disaccharides [3–5]. Thus, α-amylase inhibition remains an established approach to delay carbohydrate digestion and control postprandial glucose levels [6–8]. Oxadiazole derivatives have attracted considerable interest in drug discovery, contributing to therapies for diabetes [9], cancer [10],inflammation [11] and infectious diseases [12]. These five-membered heterocycles ($C_2H_2N_2O$) occur in four isomeric forms-1,3, 4-, 1,2,5-, 1,2,4-, and 1,2,3-oxadiazoles [13] (Fig. 1) and they and serve as versatile scaffolds, acting as pharmacophores, aromatic linkers, and hydrogen-bond [14–16]. Among them, the 1,3,4-oxadiazole scaffold

* Corresponding author.
E-mail address: ajaykumar@ycm.uni.-mysore.ac.in (K.A. Kumar).

https://doi.org/10.1016/j.molstruc.2025.144655
Received 5 September 2025; Received in revised form 23 October 2025; Accepted 4 November 2025
Available online 5 November 2025

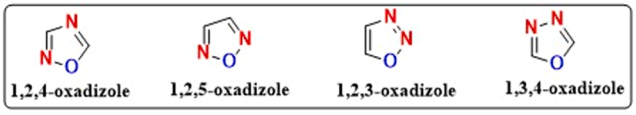

Fig. 1. Several isomeric forms of oxadiazole.

exhibits broad pharmacological activity, including anti-enzymatic [17], antibacterial [18], anticancer [19], antifungal [20], antiproliferative [21], anti-inflammatory [22], anti-diabetic [23], anti-oxidant [24], and antitubercular [25] agent. Its reduced aromaticity and –*N* = *C*–O– linkage enhance biological activity [26,27]. Furthermore, 1,3,4-oxadiazoles can inhibit α-amylase and α-glucosidase [28,29], and modulate Nrf2 pathways to strengthen antioxidant defense, promote insulin secretion, and improve glycemic control [30].

Bioisosterism is a key strategy in drug design, and pyridine-a versatile heteroaromatic ring found in many drugs-is valued for its stability, solubility, basicity, and hydrogen-bonding ability, serving as a bioisostere for amines, amides, and benzene rings [31,32]. Incorporating the pyridine nucleus often enhances pharmacological profiles, with broad therapeutic potential [33]. In antidiabetic agents, pyridine improves enzyme binding, bioavailability, and metabolic stability [34], as seen in drugs like niacin (Niacin), piroxicam, and isoniazid [35]. Secondary amines such as piperazine, morpholine, thiomorpholine, and piperidine are privileged scaffolds in drug discovery due to their prevalence and ability to enhance drug-like properties. Piperazine, second only to piperidine and pyridine in pharmaceutical importance, improves solubility, flexibility, and bioavailability [36]. Morpholine and its thio analogue, thiomorpholine, also enhance pharmacokinetics and target affinity, making them valuable pharmacophores in both approved and investigational drugs [37,38]. Piperidine remains a key heterocycle in medicinal chemistry, widely utilized in natural and synthetic derivatives

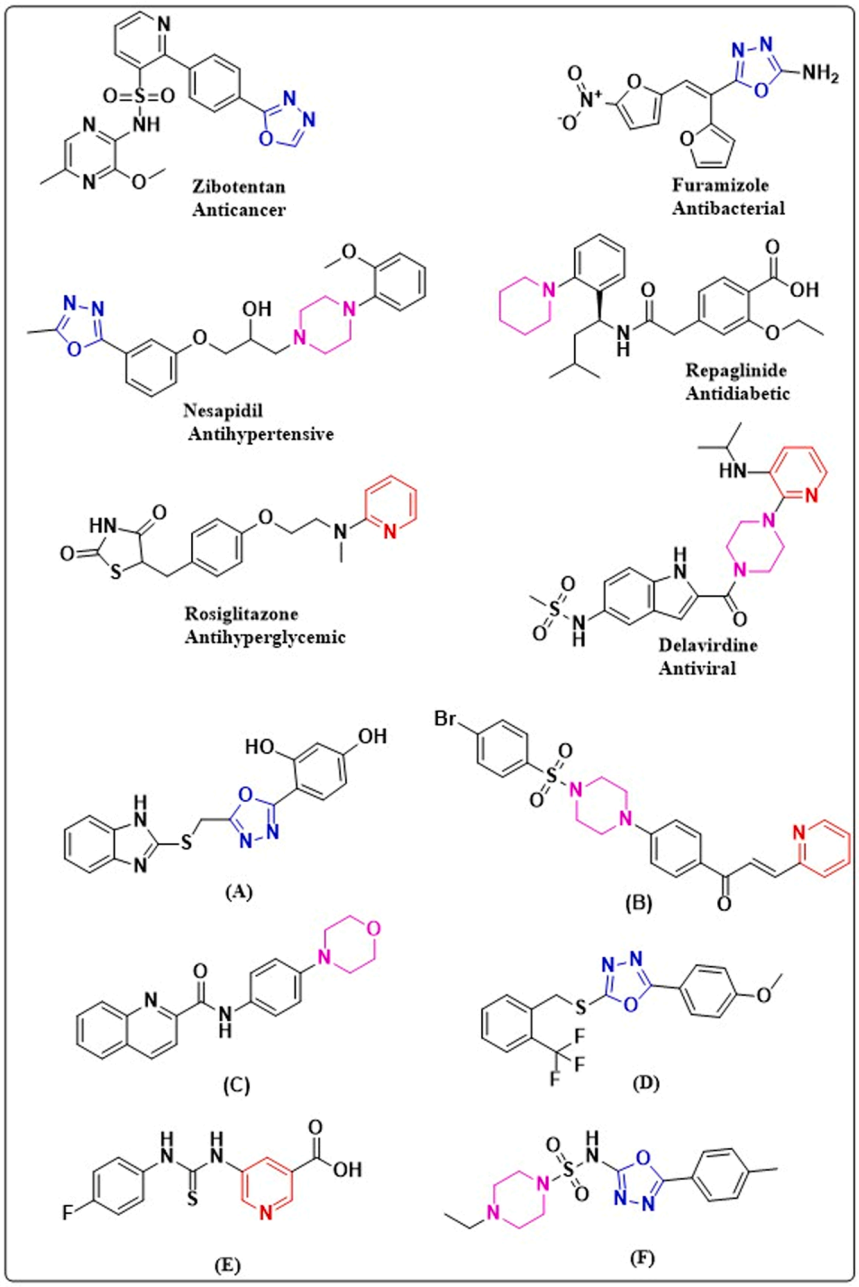

Fig. 2. Various marketed drugs and antidiabetic agents (A to F) containing 1,3,4-oxadiazole (blue), pyridine (red), and secondary amine (green) scaffolds.

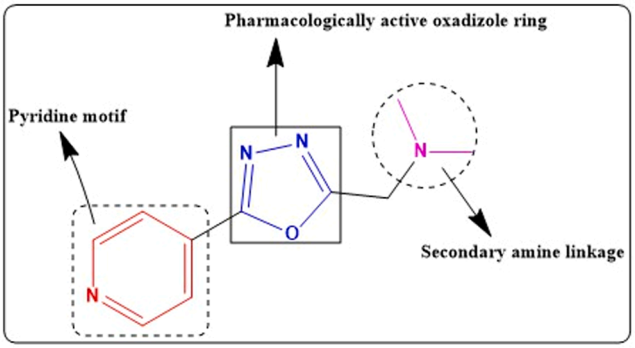

Fig. 3. Rationale for designing 1,3,4-oxadiazole derivatives decorated with secondary amines.

Table 1
Crystal data and structure refinement of the compound **5c**.

CCDC deposit No.	2479455
Empirical formula	$C_{16}H_{17}N_7O$
Formula weight	323.36
Temperature (K)	293(2)
Wavelength (Å)	0.71073
Crystal system, space group	Orthorhombic Pccn , $P2_1/c$
Unit cell dimensions	39.277(2)
a (Å)	10.8147(6)
b (Å)	7.4939(4))
c (Å)	
Volume Å^3	3183.1(3)
Z	8
Density(calculated)/ g cm^3	1.350
Absorption-coefficient (mm^{-1})	0.092
F_{000}	1360
Crystal size (mm)	0.24 × 0.22 × 0.22
θ range for data collection	3.906 ° to 56.166°
Index ranges	-49 ≤ *h* ≤ 50 -14 ≤ *k* ≤ 13 -9 ≤ *l* ≤ 9
Reflections collected	20,893
Independent reflections	3732 [R_{int} = 0.0252]
Refinement method	Full matrix least-squares on F^2
Data/restraints/parameters	3732/0/218
Goodness of fit on F^2	1.076
Final [$I > 2\sigma(I)$]	$R1$ = 0.0476, $wR2$ = 0.1268
R indices (all data)	$R1$ = 0.0730, $wR2$ = 0.1411
Largest diff. peak and hole	0.27and -0.18 eÅ^{-3}

for diverse therapeutic applications [39].

Recent studies have identified pyridine, oxadiazole, piperazine, and morpholine frameworks as promising α-amylase inhibitors (Fig. 2). Hayat Ullah *et. al.,* reported oxadiazole-benzimidazole hybrids with potent activity (IC_{50} = 5.50 ± 0.30–23.50 ± 0.30 μM), where compound A (IC_{50} = 5.50 ± 0.30 μM) surpassed acarbose (IC_{50} = 11.12 ± 0.15 μM) [40]. Narges Hosseini Nasab *et. al.,* synthesized chalcone-sulfonyl piperazine hybrids, with compound B showing the strongest inhibition (IC_{50} = 4.51 ± 1.15 μM) compared to acarbose (IC_{50} = 30.97 ± 2.91 μM) [41]. Rajendran Nithyabalaji et. al., developed phenylmorpholine-heterocyclic amides, with compound C exhibiting 85 % inhibition across all concentrations, comparable to acarbose [42]. Syeda Shamila Hamdani *et. al.,* reported 1,3,4-oxadiazole derivatives, with compound D showing the highest activity (IC_{50} = 86.83 ± 0.23 μg/mL) [43]. Muhammad Nawaz *et. al.,* synthesized 5-amino-nicotinic acid derivatives, and compound E showed strong inhibition (IC_{50} = 12.17 ± 0.14 μg/mL) comparable to acarbose (IC_{50} = 10.98 ± 0.03 μg/mL) [44]. Swarna Bharathi Kalli *et. al.,* reported piperazine-linked oxadiazole derivatives as DPP-4 inhibitors; compound F showed 27.32 % inhibition at 10 μmol/L and reduced glucose levels in STZ-induced diabetic rats [45]. The rationale behind this framework, which piqued our interest, is to employ a molecular hybridization strategy combining pyridine and 1,3,4-oxadiazole scaffolds with secondary amines like piperazine to enhance α-amylase inhibition and antidiabetic potential (Fig. 3).

Computational approaches such as molecular docking, ADME prediction, and Density Functional Theory (DFT) studies are essential in modern drug discovery. Docking assesses protein-ligand interactions and binding affinities [46], ADME profiling predicts pharmacokinetic behaviour and drug-likeness [47], and DFT links electronic structure to pharmacological activity through HOMO-LUMO and related parameters, providing insights into potential active sites [48]. Taking these points into account, herein we report the design and synthesis of 1,3,4-oxadiazole derivatives via a molecular hybridization approach, characterized by spectroscopic and computational studies, and evaluated for α-amylase inhibition to explore their potential as novel small-molecule antidiabetic agents.

2. Materials and methods

The progress of each reaction was monitored regularly by thin-layer chromatography (TLC) on Merck silica gel 60 F_{254} precoated plates, using a mixture of ethyl acetate and hexane as the mobile phase. Spots were visualized under UV light. Nuclear magnetic resonance (NMR) spectra, including ^{1}H (400 MHz) and ^{13}C (101 MHz), were recorded on an Agilent NMR spectrometer with $CDCl_3$ as the solvent and tetramethylsilane (TMS) as the internal standard. Chemical shifts (δ) are reported in parts per million (ppm). High-resolution mass spectra (HRMS) were recorded on a Waters Xevo G3 QTof instrument using electrospray ionization (ESI) in positive mode. Melting points were measured using the open capillary method. All chemicals and solvents were of analytical grade and purchased from commercial suppliers, and were used directly without further purification.

3. Experimental methodology

3.1. Synthesis of 4-Pyridinyl-1,3,4-oxadiazole compounds

To a solution of pyridine-4-carboxylic acid (compound **1**, 1 mmol) in ethanol, concentrated sulfuric acid (0.2 mmol) was added dropwise, and the mixture was heated under reflux for 8 h. After completion, the reaction was cooled, the solvent removed under reduced pressure, and the residue neutralized with aqueous sodium bicarbonate, followed by extraction with ethyl acetate (3 × 10 mL). The combined organic layers were dried over anhydrous sodium sulfate and concentrated to give the ethyl ester (compound **2**), which was then refluxed with hydrazine hydrate (1.2 mmol) in ethanol for 6 h. Progress was monitored by TLC, and after completion, the mixture was cooled, excess hydrazine removed by aqueous washing, and the precipitated solid was collected by filtration and dried to afford the acid hydrazide (compound **3**). This hydrazide (1 mmol) was subsequently reacted with monochloroacetic acid (1 mmol) in $POCl_3$ under reflux for 4 h, leading to cyclization and formation of the 2-(chloromethyl)-1,3,4-oxadiazole derivative (compound **4**). Upon completion, the reaction was quenched, neutralized with potassium carbonate, and the precipitate was filtered, washed with cold ethanol, and dried. Finally, compound 4 (1 mmol) was refluxed with the appropriate secondary amine (1 mmol), potassium carbonate (1.5 mmol), and a catalytic amount of potassium iodide (0.1 equiv) in DMF for 4 h. The reaction mixture was cooled, diluted with water, extracted with ethyl acetate, and the organic layer was dried, filtered, and concentrated under reduced pressure. The crude product was purified by

column chromatography to obtain the final 1,3,4-oxadiazole derivatives **(5a-j).**

3.2. Single crystal structural analysis

Single crystals of $C_{16}H_{17}N_7O$ (compound **5c**), suitable for X-ray diffraction analysis, were obtained by slow evaporation. A well-grown crystal was mounted on a Rigaku XtaLAB Pro II AFC12 (RINC) Kappa diffractometer equipped with Mo-Kα radiation (λ = 0.71073 Å), and data were collected at 293(2) K. The structure was solved by Intrinsic Phasing using *SHELXT* [49] and refined using full-matrix least-squares minimization with *SHELXL* implemented in *Olex2* [50,51]. The Hydrogen atoms were placed using a riding model with fixed U_{iso}values at 1.2 for all C(H) and C (H, H) groups; CH_2 hydrogens (on C8–C12) and aromatic/amide hydrogens were refined using riding coordinates without restraints or constraints. The *Planton* and *Mercury* software were used to calculate geometrical parameters, plot the ORTEP, and packing figures. Crystal data and structure refinement, including the CCDC number, are tabulated in the Table 1 [52,53].

3.3. Hirshfeld surface analysis

Hirshfeld surface analysis is a method used to study intermolecular interactions in crystal structures and is carried out using *CrystalExplorer* software [54]. The tool creates three-dimensional surfaces based on the total electron density of a molecule and its neighbours. It defines areas where the weight function equals 0.5 to measure distances to nearby atoms inside (d_i) and outside (d_e) the surface. These distances are then used to calculate the normalized contact distance (d_{norm}). This distance is shown with colour coding: red for strong interactions, white for van der Waals interactions, and blue for weak or no interactions. Additional surfaces, like shape index and curvedness, help detect π–π and C–H…π interactions. Two-dimensional fingerprint plots from the 3D Hirshfeld surface show intermolecular contacts in detail. Distinct spikes represent specific types of interactions and also provide the percentage contributions of individual contacts to the overall crystal packing [55].

3.4. Density functional theory calculations

The structural coordinates of the molecule **5c** were used for geometry optimization to investigate its electronic and surface properties. The optimization was performed at the B3LYP (Becke three-parameter, Lee–Yang–Parr) hybrid functional level with the 6–311+G(d,p) basis set to ensure convergence to the local minimum on the potential energy surface [56,57]. All calculations were carried out using *Gaussian 16*, and the results were visualized with *GaussView 6.0.16* [58]. The computations were performed in the gas phase. Frontier molecular orbital (FMO) analysis, based on the optimized geometry, provided insights into the electronic structure of the molecule. Global chemical descriptors such as HOMO and LUMO energies, energy gap, ionization potential, electron affinity, electronegativity, and chemical hardness were derived using Koopmans' approximation, a widely accepted simplified quantum mechanical method [59]. Furthermore, the molecular electrostatic potential (MEP) map was generated to visualize the electrostatic potential distribution on the molecular surface. The MEP highlights regions likely to participate in intermolecular interactions, where red regions indicate nucleophilic sites, blue regions correspond to electrophilic sites, and green regions represent neutral zones [60].

3.5. Molecular docking studies

Molecular docking studies of the synthesized molecules were performed against four diabetes-related target proteins using *Auto-Dock 4.2.6* software [61]. The selected targets (PDB IDs: 1HNY, 1SMD, 1B2Y, and 4GQR) represent enzymes associated with different aspects of diabetes pathophysiology, as reported in previous studies. The crystal structures of these proteins were retrieved from the Protein Data Bank (PDB) and prepared by removing water molecules, adding polar hydrogen atoms, and assigning Kollman charges. The Lamarckian Genetic Algorithm (LGA) was used for conformational sampling, and docking was performed with nine independent runs per ligand to ensure convergence of binding poses. The active sites for all targets were defined around their co-crystallized ligands and verified from literature-reported binding residues.The grid box size was maintained at 40 × 40 × 40 Å and centered at $x = 8.450$, $y = 58.661$, $z = 19.220$ for 1HNY, $x = 8.349$, $y = 58.705$, $z = 19.096$ for 1SMD, $x = 17.982$, $y = 21.308$, $z = 49.349$ for 1B2Y, and $x = 8.439$, $y = 28.104$, $z = 49.184$ for 4GQR, respectively, for all the ligands including the reference compound docked to the target proteins. Docking validation was carried out using the 4GQR protein as a representative system; the co-crystallized ligand reproduced its experimental conformation with an RMSD of 0.92 Å, confirming the reliability of the docking parameters and overall protocol. The docking poses and binding-site interactions were analyzed using AutoDock Tools and *Discovery Studio Visualizer* [62] to generate 2D/3D interaction maps. For comparative evaluation, acarbose, a clinically established α-amylase inhibitor, was docked against the same targets, and the binding affinities of the synthesized compounds were interpreted relative to acarbose.

3.6. In silicoADME analysis

The more affordable and quicker way of predicting the ADME properties of the compounds is the *in-silico* techniques which has gained wider acceptance worldwide [63]. The SwissADME web server was employed to evaluate the pharmacokinetic profile of the synthesized compound [64]. Key drug-likeness parameters such as molecular weight, H-bond donors and acceptors, and logP values were assessed in accordance with Lipinski's Rule of Five. Additional properties including lipophilicity, aqueous solubility, polarity, and saturation were also examined. The oral bioavailability of the compound was further investigated using the bioavailability radar and the BOILED-Egg model. In the radar plot, the shaded region indicates the optimal physicochemical space for oral bioavailability.

3.7. In vitroα-Amylase inhibition assay

3.7.1. Preparation of enzymes

Sheep pancreas was collected from a slaughterhouse and stored in cold phosphate-buffered saline (PBS). The fresh tissue was cut into small pieces, macerated under cold conditions with PBS, and homogenized using a tissue homogenizer. The homogenate was centrifuged at 10,000 rpm for 5 min in a refrigerated centrifuge, and the resulting supernatant was used for protein estimation and served as the source of α-amylase. Enzyme activity was determined using starch as the substrate, where one unit of α-amylase activity was defined as the amount of enzyme required to release 1 μmol of reducing sugar (as maltose) per minute under the assay conditions.

3.7.2. α-Amylase inhibitory assay

The synthesized analogues were evaluated against α-amylase according to the previously described method and compared with acarbose as a positive control [65]. Test compounds were prepared at concentrations ranging from 10 to 100 μg/mL. In each assay tube, 0.5 mL of 1 % starch solution and 1.5 mL of 0.01 M phosphate buffer (pH 6.9) containing α-amylase (100 μg/mL) were added, followed by incubation at room temperature for 30 min. The reaction was terminated by adding 2 mL of 2 N NaOH and 1 mL of dinitrosalicylic acid (DNS) reagent. The mixtures were then heated at 80 °C for 10 min, cooled to room temperature, and the absorbance was measured at 540 nm using a spectrophotometer. Parallel experiments were carried out using a blank (without sample) and a positive control (buffer with acarbose). The α-amylase inhibition efficiency was validated via the following

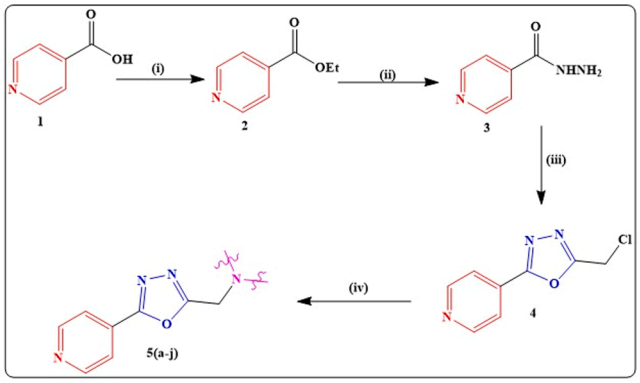

Scheme 1. Synthesis of 4-Pyridinyl-1,3,4-oxadiazoles **5(a-j); Reaction conditions**: (i) Conc.H_2SO_4, EtOH, reflux, 8 hrs. (ii) $NH_2NH_2.H_2O$, EtOH, reflux,6 hrs. (iii) $ClCH_2COOH$ (1 eq), $POCl_3$, 100 °C, 4 hrs. (iv) Different secondary amines, K_2CO_3, KI, DMF, reflux, 5 hrs.

equation:

$$\%\text{Inhibition} = \frac{\text{Control} - \text{Test sample}}{\text{Control}} \times 100$$

The concentration of the tested compounds required to produce 50 % inhibition (IC_{50}) was determined from plots of percentage inhibition *versus* log inhibitor concentration and calculated by non-linear regression analysis from the mean inhibitory values. The experiments were performed in triplicates; results are expressed as mean ± standard deviation (SD).

3.7.3. α-Amylase inhibition assay to understand the nature of inhibition

In this assay, 100 μg/mL of α-amylase enzyme was incubated in test tubes with 30 μg/mL of inhibitor and varying concentrations of substrate (1 % starch; 5, 10, 15, 20, and 25 mg/mL) at 30 °C for 30 min. The reaction was terminated by adding 2 mL of 2 N NaOH and 1 mL of dinitrosalicylic acid (DNS) reagent, followed by heating in a boiling water bath for 10 min. After cooling to room temperature, the absorbance was recorded at 540 nm. Acarbose was used as the reference control. The percentage inhibition was calculated using the following equation:

$$\%\ \text{of Inhibition}(\alpha - \text{Amylase}) = \left(\frac{\text{Blank} - \text{Sample}}{\textit{Sample}}\right) \times 100$$

3.7.4. Kinetic analysis

To gain insight into the inhibitory mechanism of the synthesized compounds on α-amylase, an enzyme kinetics study was conducted. Lineweaver–Burk plots were constructed from the α-amylase inhibition assay using starch as the substrate at varying concentrations (5, 10, 15, 20, and 25 mg/mL). The enzyme concentration (100 μg/mL) and inhibitor concentration (30 μg/mL) were kept constant. The type of inhibition was determined from the Lineweaver–Burk plots, in these plots, V_o represents the initial reaction rate, Km the Michaelis–Menten constant, Km/Vmax the slope, and 1/Vmax the y-intercept.

4. Results and discussion

4.1. Chemistry

A series of novel 4-pyridinyl-1,3,4-oxadiazole derivatives **(5a–j)** were synthesized through a multistep protocol. Initially, pyridine-4-carboxylic acid was esterified in ethanol using concentrated H_2SO_4 as a catalyst to afford the corresponding ester, which upon treatment with hydrazine hydrate yielded the acid hydrazide. Subsequent cyclization with monochloroacetic acid in the presence of $POCl_3$ furnished the chloromethyl-1,3,4-oxadiazole intermediate. Final derivatives **(5a–j)** were obtained via nucleophilic substitution of this intermediate with various secondary amines in DMF using K_2CO_3 and catalytic KI under reflux conditions. The reactions proceeded smoothly, as confirmed by TLC, and afforded the desired products in good yields (80–92 %). Purification was carried out by column chromatography using ethyl acetate-hexane mixtures as eluents. Structures of the synthesized compounds were established by spectroscopic analyses (^{1}H NMR, ^{13}C NMR), while the molecular structure of **5c** was further confirmed by single-crystal X-ray diffraction. A schematic representation of synthetic route is shown in Scheme 1. The chemical structures of the synthesised compounds **(5a-j)** are provided in Supplementary **Fig. S1.**

4.2. Spectral data of the 1,3,4-oxadiazole derivatives (compounds 5a-j)

After purification, the structures of the synthesized compounds (**5a–5j**) were confirmed by ^{1}H and ^{13}C NMR spectroscopy and mass spectrometry and the corresponding spectra are provided in the Supplementary file. In all compounds, the pyridine moiety displayed a characteristic set of four aromatic protons: two downfield doublets at δ 8.80–8.85 ppm (J = 4.4–4.7 Hz, 2H) and δ 7.91–7.95 ppm (J = 1.5–1.7 Hz, 2H), consistent with the pyridine-4-yl substitution pattern. A distinctive methylene bridge (–CH_2–) connecting the secondary amine to the oxadiazole C2 consistently resonated as a singlet at δ 3.88–4.07 ppm (2H), with slight deshielding variations across the series, and the corresponding carbons appeared at δ 52.0–54.5 ppm in the ^{13}C NMR spectra. For the piperazine-substituted derivatives (**5a, 5b, 5c**, and **5i**), the ring methylene protons resonated as two sets of triplets at δ 2.70–3.25 ppm (8H total, $J \approx$ 4.4–5.0 Hz), together with aromatic substituent protons from phenyl (**5a**), p-tolyl (**5b**), pyrimidyl (**5c**), or dichlorophenyl (**5i**). Compounds with other secondary amine substituents (**5d, 5e, 5f, 5 *g*, 5h**, and **5j**) showed distinct aliphatic patterns: the piperidine derivatives (**5d** and **5e**) had multiplets at δ 1.45–3.00 ppm, with **5e** also showing a carbonyl carbon at δ 207.5 ppm; morpholine (**5f**) and thiomorpholine (**5 *g***) displayed triplets between δ 2.63–3.94 ppm; compound **5h** gave a tert-butyl singlet at δ 1.43 ppm (9H) with multiple aliphatic multiplets at δ 1.04–2.96 ppm; while **5j** exhibited aromatic multiplets at δ 7.16–7.47 ppm alongside aliphatic signals at δ 2.12–3.92 ppm. The ^{13}C NMR spectra of all derivatives further confirmed the successful formation of the 1,3,4-oxadiazole core, with C2 and C5 carbons consistently at δ 163.5–165.0 ppm, pyridine carbons between δ 120.2–151.1 ppm, and substituent-specific signals such as the p-tolyl methyl carbon (**5b**, δ 20.5 ppm), morpholine O-CH_2 (**5f**, δ 66.8 ppm), tert-butyl carbon (**5h**, δ 79.2 ppm), and diphenyl carbons (**5j**, δ 125.9–128.4 ppm). Additionally, the mass spectra of all compounds (**5a–5j**) show molecular ion peaks ([M + H] $^+$) consistent with their calculated molecular weights. Overall, the observed chemical shifts, multiplicities, and coupling constants across both ^{1}H and ^{13}C NMR spectra were fully consistent with the proposed structures, confirming the successful synthesis of the pyridine-linked 1,3,4-oxadiazole derivatives (**5a–5j**).

- 2-((4-phenylpiperazin-1-yl)methyl)-5-(pyridin-4-yl)-1,3,4-oxadiazole (5a)

White solid; mp:186–188 °C; Yeild: 89 %; ^{1}H NMR (400 MHz, $CDCl_3$) ^{1}H NMR (400 MHz, $CDCl_3$) δ 8.83 (dd, J = 4.5, 1.6 Hz, 2H), 7.94 (dd, J = 4.5, 1.6 Hz, 2H), 7.29–7.26 (m, 2H), 6.94–6.91 (m, 2H), 6.87 (tt, J = 7.3, 1.0 Hz, 1H), 3.99 (s, 2H), 3.25 (t, J = 5.0 Hz, 4H), 2.81 (t, J = 5.0 Hz, 4H). ^{13}C NMR (101 MHz, $CDCl_3$) δ 164.4, 163.8, 151.1, 151.0, 130.9, 129.3, 120.5, 120.2, 116.4, 77.5, 77.2, 76.8, 53.0, 52.1, 49.2. HRMS (ESI^+) calculated for $C_{18}H_{19}N_5O$ + *H*: 322.1668 ([M + H]$^+$). Found:322.1975 [M + H]$^+$.

- 2-(pyridin-4-yl)-5-((4-(p-tolyl)piperazin-1-yl)methyl)-1,3,4-oxadiazole (5b)

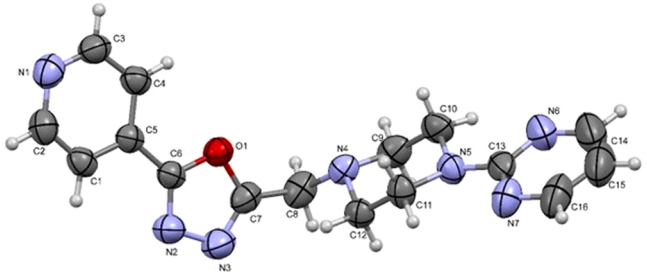

Fig. 4. The ORTEP of the compound **5c** with thermal ellipsoid drawn at 50 % probability.

White solid; mp:144–146 °C; Yield: 85 %; ^{1}H NMR (400 MHz, $CDCl_3$) δ 8.82 (dd, J = 4.4, 1.7 Hz, 2H), 7.94 (dd, J = 4.4, 1.7 Hz, 2H), 7.07 (dd, J = 6.5, 2.1 Hz, 2H), 6.84 (dd, J = 6.2, 2.2 Hz, 2H), 3.98 (s, 2H), 3.19 (t, J = 5.0 Hz, 4H), 2.81 (t, J = 5.0 Hz, 4H), 2.26 (s, 3H). ^{13}C NMR (101 MHz, $CDCl_3$) δ 164.4, 163.8, 151.0, 149.0, 131.0, 129.8, 129.7, 120.5, 116.7, 77.5, 77.2, 76.8, 53.1, 52.1, 49.8, 20.5. HRMS (ESI^+) calculated for $C_{19}H_{21}N_5O$ + H: 336.1824 ($[M + H]^+$). Found:336.2172 $[M + H]^+$.

- 2-(pyridin-4-yl)-5-((4-(pyrimidin-2-yl)piperazin-1-yl)methyl)-1,3,4-oxadiazole (5c)

White crystal; mp:128–122 °C; Yield: 85 %;^{1}H NMR (400 MHz, $CDCl_3$) δ 8.82 (dd, J = 4.5, 1.6 Hz, 2H), 8.30 (d, J = 4.7 Hz, 2H), 7.94 (dd, J = 4.5, 1.6 Hz, 2H), 6.50 (t, J = 4.7 Hz, 1H), 3.98 (s, 2H), 3.89 (t, J = 5.0 Hz, 4H), 2.71 (t, J = 5.0 Hz, 4H). ^{13}C NMR (101 MHz, $CDCl_3$) δ 164.4, 163.8, 161.6, 157.8, 151.0, 131.0, 120.5, 110.2, 77.5, 77.2, 76.8, 52.9, 52.2, 43.5. HRMS (ESI^+) calculated for $C_{16}H_{17}N_7O$ + H: 324.1573 ($[M + H]^+$). Found:324.1772 $[M + H]^+$

- 2-(piperidin-1-ylmethyl)-5-(pyridin-4-yl)-1,3,4-oxadiazole (5d)

Light brown solid; mp: 188–190 °C; Yield: 92 %; ^{1}H NMR (400 MHz, $CDCl_3$) δ 8.81 (dd, J = 4.4, 1.4 Hz, 2H), 7.93 (dd, J = 4.5, 1.6 Hz, 2H), 3.88 (s, 2H), 2.56 (t, J = 5.3 Hz, 4H), 1.66–1.60 (m, 4H), 1.45 (q, J = 5.9 Hz, 2H). ^{13}C NMR (101 MHz, $CDCl_3$) δ 164.9, 163.7, 151.0, 131.1, 120.6, 77.5, 77.2, 76.8, 54.4, 52.9, 29.8, 29.8, 25.9, 23.8. HRMS (ESI^+) calculated for $C_{12}H_{14}N_4O_2$ + H: 245.1402 ($[M + H]^+$). Found:245.1421 $[M + H]^+$

- 1-((5-(pyridin-4-yl)-1,3,4-oxadiazol-2-yl)methyl)piperidin-4-one (5e)

Light brown solid; mp: 116–118 °C; Yield: 86 %; ^{1}H NMR (400 MHz, $CDCl_3$) δ 8.85 (dd, J = 4.5, 1.6 Hz, 2H), 7.95 (dd, J = 4.5, 1.6 Hz, 2H), 4.07 (s, 2H), 3.00–2.95 (m, 4H), 2.54 (t, J = 6.2 Hz, 4H). ^{13}C NMR (101 MHz, $CDCl_3$) δ 207.5, 164.4, 163.8, 151.0, 130.9, 120.6, 77.5, 77.2, 76.8, 52.9, 51.5, 41.1, 29.8, 29.8. HRMS (ESI^+) calculated for $C_{13}H_{14}N_4O_2$ + H: 259.1195 ($[M + H]^+$). Found:259.1181 $[M + H]^+$

- 4-((5-(pyridin-4-yl)-1,3,4-oxadiazol-2-yl)methyl)morpholine (5f)

Dark brown solid; mp: 194–196 °C; Yield: 80 %; ^{1}H NMR (400 MHz, $CDCl_3$) δ 8.81 (dd, J = 4.4, 1.7 Hz, 2H), 7.91 (dd, J = 4.4, 1.7 Hz, 2H), 3.89 (s, 2H), 3.74 (t, J = 4.7 Hz, 4H), 2.63 (t, J = 4.7 Hz, 4H). ^{13}C NMR (101 MHz, $CDCl_3$) δ 164.3, 163.8, 151.0, 131.0, 120.6, 77.5, 77.2, 76.8, 66.8, 53.4, 52.5, 29.8. HRMS (ESI^+) calculated for $C_{13}H_{16}N_4O$ + H: 247.1195 ($[M + H]^+$). Found:247.1145 $[M + H]^+$

- 2-(pyridin-4-yl)-5-(thiomorpholinomethyl)-1,3,4-oxadiazole (5 g)

White solid; mp: 188–190 °C; Yield: 82 %; ^{1}H NMR (400 MHz, $CDCl_3$) δ 8.83 (dd, J = 4.5, 1.6 Hz, 2H), 7.92 (dd, J = 4.4, 1.7 Hz, 2H), 3.94 (s, 2H), 2.91–2.89 (m, 4H), 2.73–2.71 (m, 4H). ^{13}C NMR (101 MHz, $CDCl_3$) δ 164.4, 163.8, 151.0, 131.0, 120.5, 77.5, 77.2, 76.8, 54.7, 53.0, 28.0. HRMS (ESI^+) calculated for $C_{12}H_{14}N_4OS$ + H: 263.0966 ($[M + H]^+$). Found:263.1076 $[M + H]^+$

- tert-butyl-4-(3-(1-((5-(pyridin-4-yl)-1,3,4-oxadiazol-2-yl)methyl) piperidin-4-yl)propyl)piperidine-1-carboxylate (5 h)

White solid; mp:128–130 °C; Yield: 90 %; ^{1}H NMR (400 MHz, $CDCl_3$) δ 8.80 (dd, J = 4.5, 1.6 Hz, 2H), 7.92 (dd, J = 4.4, 1.7 Hz, 2H), 4.05 (d, J = 7.8 Hz, 2H), 3.89 (s, 2H), 2.96 (d, J = 11.6 Hz, 2H), 2.64 (t, J = 12.2 Hz, 2H), 2.18 (t, J = 11.2 Hz, 2H), 1.68 (d, J = 10.5 Hz, 2H), 1.60 (d, J = 13.3 Hz, 2H), 1.43 (s, 9H), 1.28–1.19 (m, 10H), 1.04 (qd, J = 12.3, 4.1 Hz, 2H). ^{13}C NMR (101 MHz, $CDCl_3$) δ 164.8, 163.5, 154.9, 150.8, 131.1, 120.5, 79.2, 77.5, 77.4, 77.2, 76.8, 53.8, 52.4, 44.1, 36.7, 36.6, 36.0, 35.1, 32.2, 32.1, 29.7, 28.5, 23.7, 21.2. HRMS (ESI^+) calculated for $C_{26}H_{39}N_5O_3$ + H: 470.3131 ($[M + H]^+$). Found:470.3314 $[M + H]^+$

- 2-((4-(2,3-dichlorophenyl)piperazin-1-yl)methyl)-5-(pyridin-4-yl)-1,3,4-oxadiazole (5i)

Light yellow solid; mp: 156–158 °C; Yield: 91 %; ^{1}H NMR (400 MHz, $CDCl_3$) δ 8.83 (dd, J = 4.5, 1.5 Hz, 2H), 7.95 (dd, J = 4.5, 1.6 Hz, 2H), 7.18–7.12 (m, 2H), 6.95 (dd, J = 7.3, 2.3 Hz, 1H), 4.00 (s, 2H), 3.12 (t, J = 4.4 Hz, 4H), 2.85 (t, J = 4.4 Hz, 4H). ^{13}C NMR (101 MHz, $CDCl_3$) δ 164.4, 163.7, 150.9, 134.1, 130.9, 127.6, 127.6, 124.9, 120.5, 118.7, 77.5, 77.2, 76.8, 53.1, 52.1, 51.1. HRMS(ESI^+) calculated for $C_{18}H_{17}Cl_2N_5O$+H: 390.0888 ($[M + H]^+$). Found:390.1098 $[M + H]^+$

- diphenyl(1-((5-(pyridin-4-yl)-1,3,4-oxadiazol-2-yl)methyl)piperidin-4-yl)methanol (5j)

White solid; mp: 190–192 °C; Yeild: 90 %; ^{1}H NMR (400 MHz, $CDCl_3$) δ 8.81 (dd, J = 4.4, 1.7 Hz, 2H), 7.92 (dd, J = 4.5, 1.6 Hz, 2H), 7.47–7.44 (m, 4H), 7.31–7.27 (m, 4H), 7.20–7.16 (m, 2H), 3.92 (s, 2H), 3.03 (d, J = 11.6 Hz, 2H), 2.32–2.26 (m, 2H), 2.12 (s, 1H), 1.57–1.52 (m, 4H). ^{13}C NMR (101 MHz, $CDCl_3$) δ 164.7, 163.7, 151.0, 145.8, 131.1, 128.4, 126.8, 125.9, 120.6, 79.6, 77.5, 77.2, 76.8, 53.9, 52.2, 43.8, 26.5. HRMS (ESI^+) calculated for $C_{26}H_{26}N_5O$ + H: 427.2134 ($[M + H]^+$). Found:427.2441 $[M + H]^+$

4.3. Single crystal X-ray structural analysis

The molecular structure of compound **5c** was confirmed by single-crystal X-ray diffraction (Fig. 4). The ORTEP diagram reveals the presence of four distinct ring systems. At one end, the pyridine ring (N1–C1–C2–C3–C4–C5) is directly bonded to the oxadiazole ring (C5–C6–O1–N3–N2), forming a fused, non-conjugated aromatic segment.

From the oxadiazole moiety, a side chain extending through C8 connects to the piperazine ring (N4–C9–C10–N5–C11–C12) via a dihedral angle of 111.08°, indicating a nearly perpendicular orientation and overall non-planar geometry. The piperazine ring adopts a puckered chair conformation, as evidenced by deviations from the mean plane (–0.2485 to +0.2686 Å) and Cremer–Pople parameters (Q = 0.5594 Å, θ = 7.47°). This confirms the chair geometry, with all atoms predominantly sp^3 hybridized except N5, which shows sp^2 character due to partial conjugation with the adjacent diazine system.

The terminal 1,2-diazine ring is connected via C13 to N5 of the piperazine moiety. Intermolecular interactions further stabilize the packing: $R_2^2(24)$ ring synthons are formed by C10–H10B···N1 hydrogen bonds, which propagate into a one-dimensional chain through C15–H15···C13 interactions (Fig. 5). Additional weak contacts, summarized in Table 2, contribute to the stabilization of the crystal lattice.

These findings confirm the successful formation of the designed

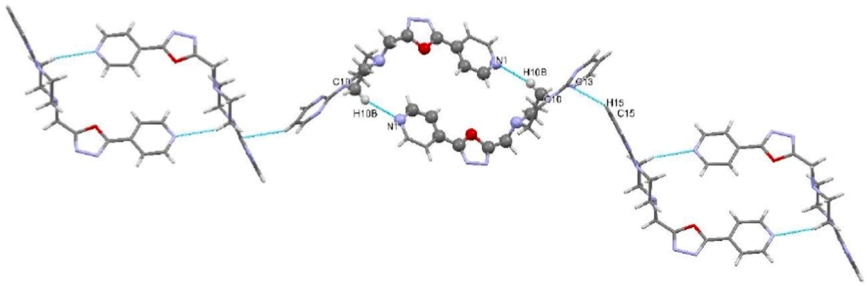

Fig. 5. The $R_2^2(24)$ ring synthons are interconnected to form a 1-D chain.

Table 2
Geometry of intermolecular interactions of the compound.

Sl. No.	D-H…A	D-H (Å)	H…A (Å)	D-A (Å)	D-H…A ()
1.	C15-H15…C13	0.93	2.651(	3.675(1)	142.99
2.	C10-H10B…N1	0.97	2.730	3.651(1)	158.76
3.	C12-H12B…N3	0.86	2.611	3.412(1)	140.12
4.	C1-H1…C4	0.93	2.836	3.702(2)	155.47

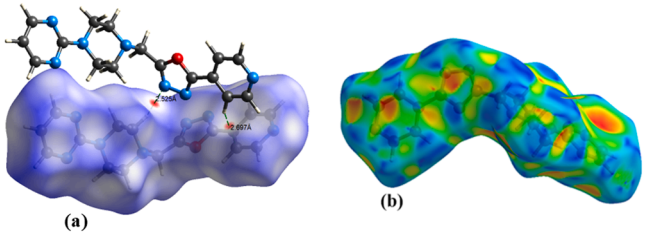

Fig. 6. **(a)** 3D d_{norm} Hirshfeld surface, **(b)** shape index of the compound.

scaffold and provide insights into its solid-state geometry and packing motifs.

4.4. Hirshfeld surface analysis

The d_{norm} Hirshfeld surface (HS) of compound **5c** reveals several prominent red spots corresponding to short intermolecular contacts (Fig. 6a). A notable interaction involves C15–H15···C13 within the diazine moiety, while additional red regions highlight C10–H10···N1 (piperazine···pyridine), C12–H12B···N3 (piperazine···oxadiazole), and an intramolecular C1–H1···C4 contact in the pyridine ring. Fig. 6a also depicts the intermolecular contacts with the nearest neighbouring crystal units along with the corresponding hydrogen-bond (HB) distances, providing a clearer understanding of the packing interactions. These features corroborate the hydrogen-bond synthons identified in the crystallographic analysis.

The shape-index surface further supports the presence of π–π stacking, displaying characteristic red and blue triangle pairs (bow-tie pattern) around the aromatic centroids Cg1 (O1–C6–N2–N3–C7) and Cg2 (N1–C1–C2–C3–C4–C5) (Fig. 6b). The centroid-to-centroid distance of 3.5859(10) Å, with a slippage of 1.65(9) Å, indicates a significant face-to-face π–π interaction. This is reinforced by the small interplanar angle (1.286°) and short interatomic contacts (3.3829(6) Å, 3.3474(7) Å), confirming well-aligned and stable stacking interactions in the lattice. Together, these Hirshfeld surface and fingerprint plot analyses confirm that the crystal packing of **5c** is stabilized not only by localized C–H···N/C interactions but also by appreciable π–π stacking, consistent with the observed supramolecular assembly.

The 2D fingerprint plots provide a quantitative overview of the intermolecular contacts within the crystal (Fig. 7). The dominant interactions are H···H contacts (45.4 %), which appear as a broad, intense central peak at $d_i = d_e \approx 1.1$ Å. H···N interactions (28.7 %) constitute the

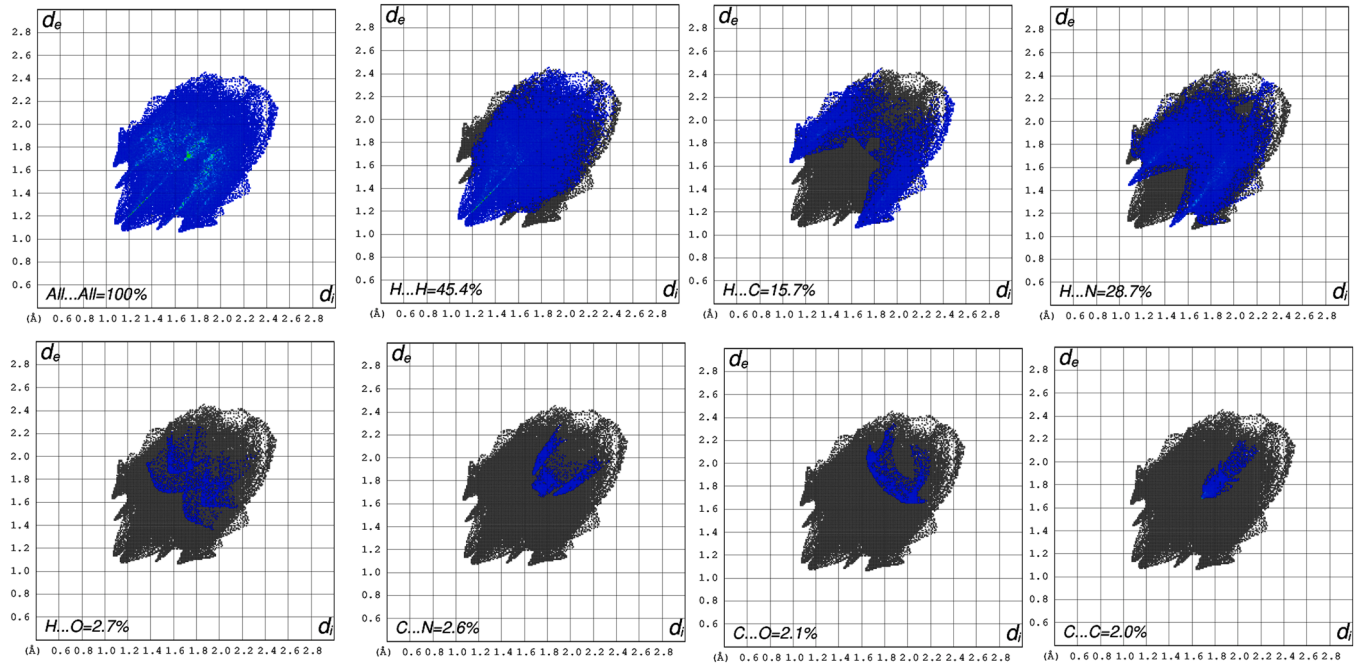

Fig. 7. 2D fingerprint plot derived from Hirshfeld surface.

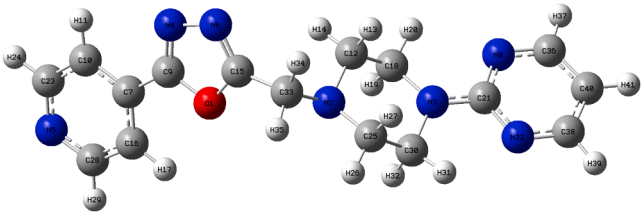

Fig. 8. DFT optimized structure of the compound **5c.**

Table 3
Chemical reactive descriptors of the compound **5c.**

Parameter	Values
E_{HOMO} (eV)	-6.1677
E_{LUMO} (eV)	-2.2694
Energy gap	3.8983
Ionization energy (I)	6.6177
Electron Affinity (A)	2.2694
Electronegativity (χ)	4.2186
Chemical Potential (μ)	-4.2186
Global hardness (η)	1.9492
Global softness (s)	0.5130
Electrophilicity index (ω)	4.5652

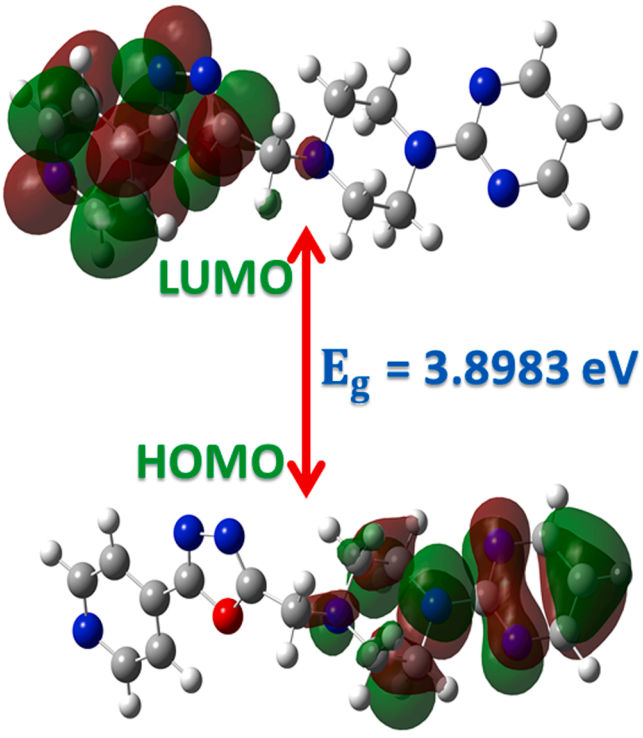

Fig. 9. Frontier molecular orbital energies of compound **5c.**

second major contribution, characterized by symmetrical diagonal streaks at $d_i + d_e \approx 3.2$ Å. H···C contacts (15.7 %) form the third most significant group, producing a characteristic "pigeon-wing" pattern at $d_i + d_e \approx 2.8$ Å. Minor contributions arise from H···O, C···N, and C···O contacts, while C···C interactions (2.0 %) reflect the presence of π–π stacking in the lattice. Overall, the fingerprint analysis confirms that hydrogen-involving contacts dominate the packing, complemented by a smaller but significant contribution from π–π interactions.

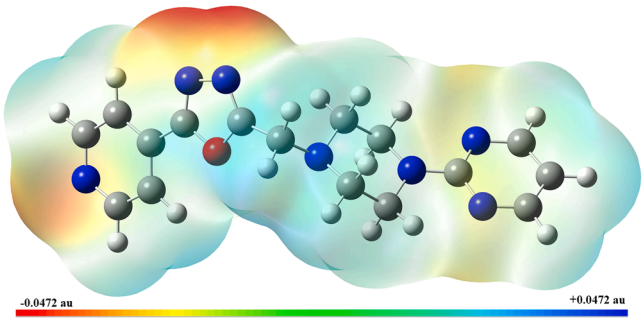

Fig. 10. Molecular electrostatic potential map of the compound **5c.**

Table 4
IC_{50} values of compounds **5a-5j** against α-amylase compared with acarbose.

Name of the Compounds	IC_{50} values (μM) [a]
Acarbose	35.8 ± 1.25
5a	141.6 ± 1.28
5b	135.3 ± 0.86
5c	106.1 ± 1.21
5d	>200
5e	>200
5f	196.0 ± 0.9
5 *g*	>200
5h	>200
5i	107.0 ± 1.81
5j	>200

[a] Values represent mean ± standard deviation (SD) (n = 3).

4.5. *Density functional theory*

The optimized geometry of compound **5c** was compared with its experimentally determined crystal structure. Experimental and theoretical bond lengths, bond angles, and torsional angles were evaluated by computing correlation coefficient values (**Supplementary Tables S1-S3**). The good correlation coefficient values observed between the experimental and calculated structure for bond lengths (0.9754), bond angles (0.9907) and torsion angles (0.9995) confirm the well comparison of the structural parameters. The optimized structure (Fig. 8) was used to study the molecular orbital energies, global and local indices and molecular electrostatic potential surface of the molecule.

The highest occupied molecular orbital (HOMO) and the lowest unoccupied molecular orbital (LUMO) are crucial for analyzing the stability and reactivity of the compound. Their energy values, along with the HOMO-LUMO gap (E_g), were computed and are listed with the global reactivity descriptors in Table 3. The HOMO and LUMO spatial plots for the optimized structure of **5c** are shown in Fig. 9. The LUMO is delocalized over the pyridine and oxadiazole moieties, whereas the HOMO is localized on the piperazine and pyrimidine moieties. The calculated HOMO–LUMO energy gap of 3.8983 eV (Fig. 9) suggests lower kinetic stability but higher chemical reactivity. Furthermore, the MEP map was generated to visualize the distribution of electrostatic potential across the molecular surface (Fig. 10). This analysis provides insights into intermolecular interactions, reactivity, and the identification of electrophilic and nucleophilic regions. The potential values range from –0.0472 a.u. to +0.0472 a.u. The red regions, concentrated over oxygen and nitrogen atoms, indicate nucleophilic sites, while the blue regions, localized around nitrogen and carbon atoms, represent electrophilic regions.

4.6. *Anti diabetic activity of the synthesied compounds 5(a-j)*

All compounds (**5a–j**) were evaluated *in vitro* for their inhibitory

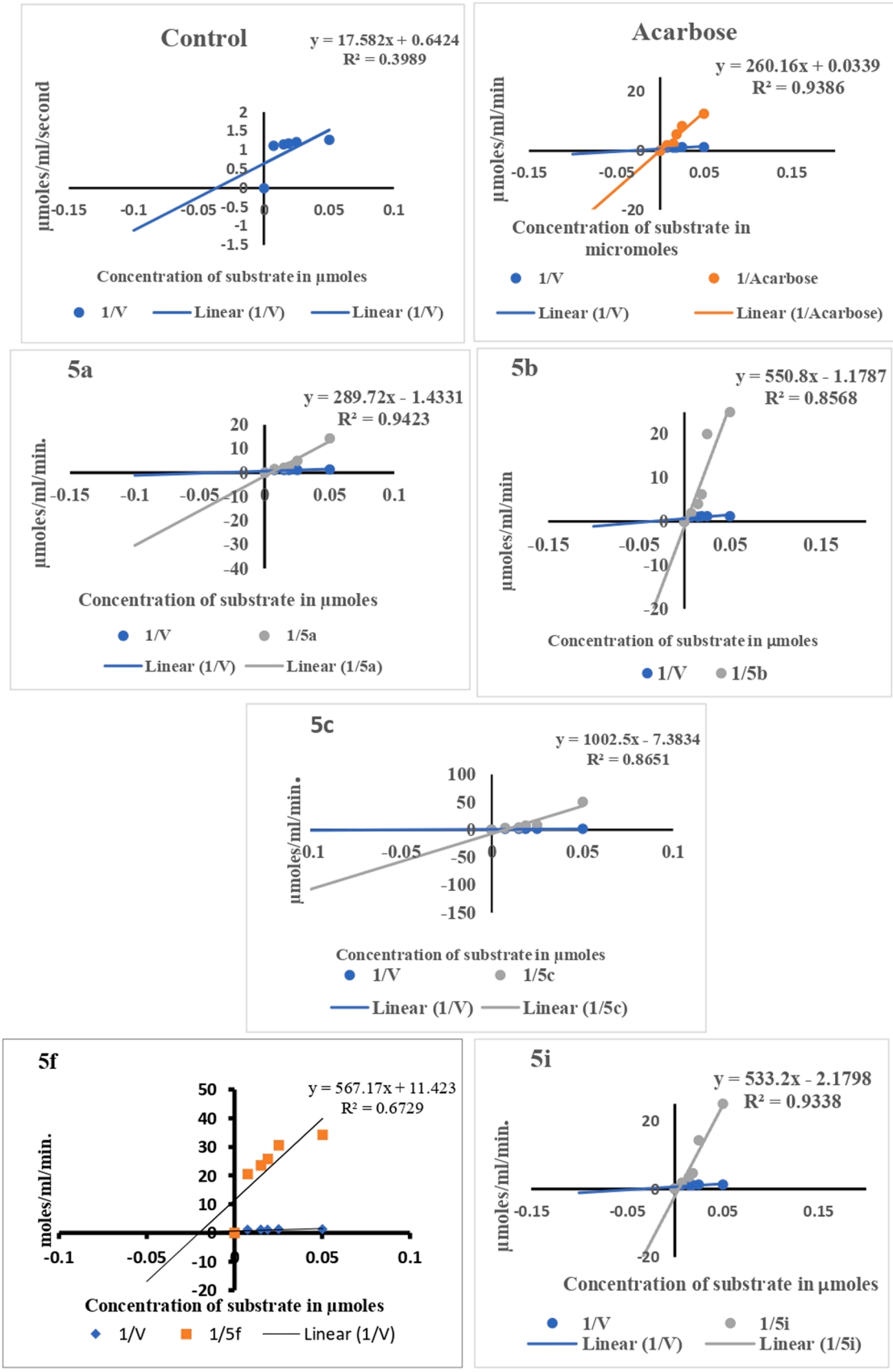

Fig. 11. The lineweaver-burk plots of the compounds **5a, 5b, 5c, 5f**, and **5i** against α-amylase.

Table 5
Inhibition kinetics of alpha amylase with tested compounds.

Name of the Compounds	K_m values in μM	V_{max} values in μM/min.
Control (without any inhibitor)	27.36	1.55
Acarbose	1670	1.55
5a	202.16	0.697
5b	467.29	0.848
5c	135.77	0.135
5f	45.34	0.080
5i	244.60	0.458

Table 6
Docking scores of compound **5c** and **acarbose** with interacting amino acid residues and hydrogen bond distances against selected targets.

Receptor	Binding Affinity (kcal·mol^{-1})		H-bonding Residues (Å)	Hydrophobic Residues	π–π stacking Residues
	Ligand (5c)	**Acarbose**			
1HNY	-7.8	-7.3	GLN63 (2.4)	TRP59, HIS201, LEU165,TYR6, PHE163	TRP59
1SMD	-7.8	-7.2	Asp300 (3.2)	LEU162,LEU165, HIS201,ILE235, ALA198	TRP59
1B2Y	-8.0	-7.0	ASP197 (3.6), GLN63 (2.6)	HIS201,LEU162, TYR62,ALA198, ILE235,HIS305, and GLU233	TRP59
4GQR	-7.7	-7.1	ASN105 (3.7), GLN63 (3.1)	TRP59,LEU165, ALA106, GLY104, GLY105	TYR62

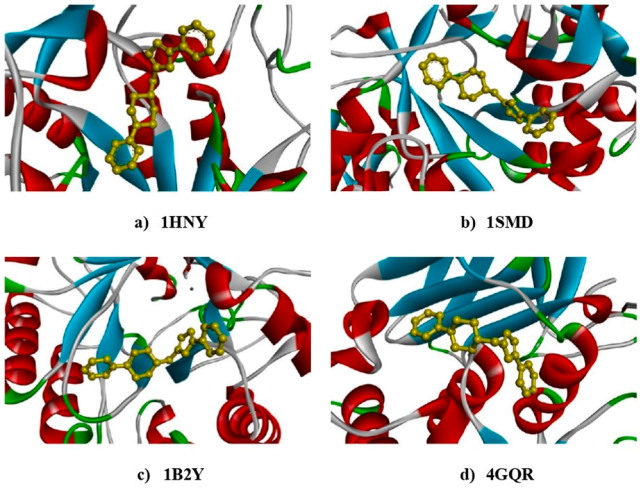

Fig. 12. 3D visualisation of the receptor-ligand interactions for the different target proteins.

activity against α-amylase. Among them only five derivatives exhibited measurable inhibition, with IC_{50} values summarized in Table 4. Acarbose was the most potent reference inhibitor (IC_{50} = 35.8 ± 1.25 μM), while within the series compound **5c** emerged as the most active (IC_{50} = 106.1 ± 1.21 μM), followed by **5i** (107.0 ± 1.81 μM) and **5b** (135.3 ± 0.86 μM). The potency of **5c** can be attributed to its unique side chain containing four nitrogen atoms, which enable strong hydrogen bonding interactions at the enzyme active site. The potency of **5c** can be attributed to its unique side chain containing four nitrogen atoms, which enables strong hydrogen-bonding interactions at the enzyme active site. Docking confirmed multiple H-bond interactions along with π–π stacking and hydrophobic contacts, yielding a good binding score. MEP analysis revealed an extended negative potential region (–0.0472 a.u.) over the side-chain nitrogens, further supporting electrostatic complementarity. Moreover, the pyrimidyl scaffold in **5c** provides lone pairs for hydrogen bonding and a conjugated aromatic system for π–π stacking, enhancing stability and affinity within the cavity. Collectively, these features explain the superior inhibitory activity of **5c**, in line with literature reports that nitrogen heteroatoms reinforce enzyme-ligand binding through hydrogen-bond interactions [66].

Preliminary structure-activity relationship (SAR) studies of the synthesized 1,3,4-oxadiazole derivatives (**5a-5j**) indicate that their inhibitory activity arises from the interplay of their structural components. All compounds share a common framework consisting of a pyridine ring, a 1,3,4-oxadiazole core, and diverse secondary amine substituents. These variations significantly influence α-amylase inhibition, as reflected by the IC_{50} values (Table 4). Five derivatives (**5a, 5b, 5c, 5f, 5i**) exhibited notable activity, whereas the others showed weak or negligible inhibition (IC_{50} > 200 μM). Cyclic secondary amines, particularly aromatic piperazines (**5a, 5b, 5c, 5i**), enhanced activity via optimal hydrogen-bonding and hydrophobic interactions. Replacement of the piperazine nitrogen distal to the oxadiazole –CH_2– linker with a heteroatom, as in **5f** (morpholine), maintained moderate activity. In contrast, modifications with –CH_2– (**5d**), –CO– (**5e**), or –S– (**5 *g***) reduced activity, highlighting the importance of nitrogen-mediated interactions. It is also evident that incorporation of N-aromatic systems further improves activity; notably, **5c**, bearing a pyrimidinyl-piperazine, showed one of the highest inhibitory effects (IC_{50} = 106.1 ± 1.21 μM), suggesting that additional nitrogen atoms enhance binding affinity. Sterically bulky groups (**5h, 5j**) diminished activity, indicating steric hindrance impedes effective binding. Overall, the electronic and steric nature of secondary amine substituents, particularly distal nitrogen or N-aromatic systems, critically modulates α-amylase inhibition. These findings are consistent with molecular docking analyses, which show stronger hydrogen-bonding and hydrophobic contacts in the most active compounds.

4.7. Kinetic analysis

Kinetic analysis was performed to elucidate the mode of inhibition of the synthesized compounds against α-amylase, using acarbose as the reference inhibitor. The Lineweaver-Burk plots and the corresponding kinetic parameters (Km and Vmax) are presented in Fig. 11 and Table 5 respectively. For the control (without inhibitor), the enzyme displayed a Km of 27.36 μM and a Vmax of 1.55 μM/min. In the presence of acarbose, Km increased markedly to 1670 μM while Vmax remained essentially unchanged at 1.55 μM/min, confirming its role as a competitive inhibitor that binds at the active site and can be displaced by higher substrate concentrations according to the law of mass action. In contrast, compounds **5a, 5b, 5c, 5f, and 5i** exhibited a distinct kinetic profile, characterized by a substantial reduction in Vmax (0.697, 0.848, 0.135, 0.080, and 0.458 μM/min, respectively) along with an increase in Km values (202.16, 467.29, 135.78, 45.34, and 244.61 μM, respectively). This trend is indicative of non-competitive inhibition, where binding at an allosteric site induces conformational changes that lower catalytic turnover and reduce substrate affinity. Collectively, these findings demonstrate that while acarbose functions as a classical competitive inhibitor, the synthesized compounds predominantly act via a non-competitive mechanism, underscoring their distinct mode of α-amylase inhibition.

4.8. Molecular docking studies

Molecular docking studies of the synthesized compounds (**5a-5j**) were conducted against four selected α-amylase target proteins (1HNY, 1SMD, 1B2Y, and 4GQR) in order to figure out the feasible binding interactions. The docking scores (binding free energies) of the synthesized compounds ranged from -6.2 to -8.2 kcal mol^{-1} across all targets, while

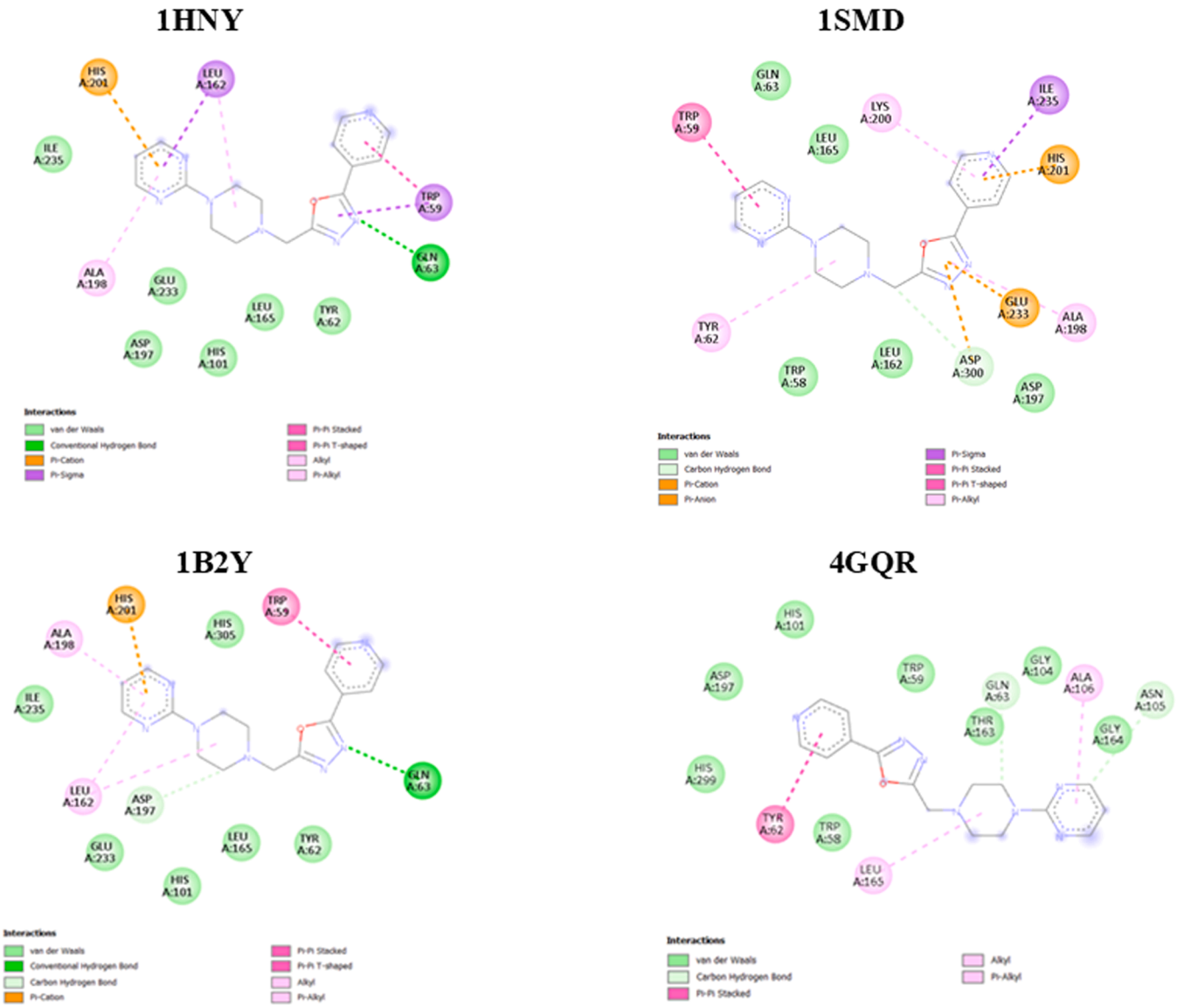

Fig. 13. 2D visualisation of the receptor-ligand interactions for the different target proteins.

Table 7
In silico ADME studies of the synthesised compound **5c.**

Parameters	
Log P (lipophilicity)	0.42
TPSA (total polar surface area, Å^2)	84.07
Molecular weight, gmol $^{-1}$	323.35
HBD (number of hydrogen bond donors)	0
HBA (number of hydrogen bond acceptors)	7
n violations (number of violated drug-likeness rules)	0
Nrotb (number of rotating bonds)	4

the reference inhibitor acarbose exhibited binding energies of -7.3, -7.2, -7.5, and -7.4 kcal mol^{-1} for 1HNY, 1SMD, 1B2Y, and 4GQR, respectively (The results are tabulated in Supplementary **Table S4**). The favorable docking scores observed for most compounds can be ascribed to the aromatic nitrogen-containing frameworks and flexible linkers, which enable efficient hydrogen bonding and optimal alignment within the α-amylase catalytic pocket, thereby enhancing interactions with key active-site residues. Among all the synthesized derivatives, compound **5c** exhibited the most favorable and consistent docking scores across the selected α-amylase targets, surpassing the reference inhibitor acarbose in most cases, indicating its strong binding affinity and potential as a potent α-amylase inhibitor. In 1HNY, **5c** binds within the catalytic pocket with a docking score of -7.8 kcal mol^{-1}, forming a hydrogen bond between the oxadiazole ring and GLN63 (2.4 Å), while a π–π stacking interaction between the pyridine–oxadiazole ring system and TRP59 contributes significantly to complex stabilization. Hydrophobic contacts involving TYR62, LEU162, LEU165, ALA198, ILE235, and GLU233 further strengthen the receptor-ligand complex and maintain the optimal ligand orientation. In 1SMD, **5c** shows a docking score of -7.8 kcal mol^{-1}, where a hydrogen bond is established between the oxadiazole ring and ASP300 (3.0 Å), supported by a π–π stacking interaction with TRP59 and hydrophobic contacts with LEU162, LEU165, HIS201, ILE235, and ALA198 that collectively stabilize the complex. For 1B2Y, the docking score is -8.0 kcal mol^{-1}, and **5c** shows the strongest binding, characterized by a hydrogen bond between the oxadiazole ring and GLN63 (2.6 Å), a prominent π–π stacking interaction between TRP59 and the terminal pyridine ring, and a carbon–hydrogen bond between the piperazine ring and ASP197 (3.6 Å). Additional hydrophobic interactions with HIS201, LEU162, TYR62, ALA198, ILE235, HIS305, and GLU233 further stabilize the receptor-ligand complex. In 4GQR, with a docking score of -7.7 kcal mol^{-1}, two carbon–hydrogen bonds are observed-one between the piperazine ring and GLN63 (3.1 Å) and

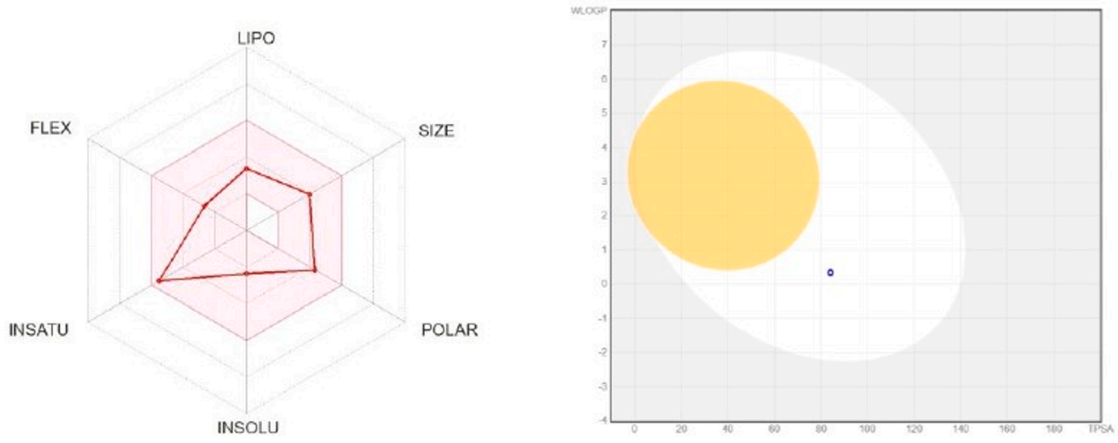

Fig. 14. **(a)** The bioavailability radar, **(b)** Boiled egg pose of the synthesized molecule.

another between the pyrimidyl ring and ASN105 (3.7 Å)-along with a π–π stacking interaction between the terminal pyridine ring and TYR62. Hydrophobic residues TRP59, LEU165, ALA106, GLY104, and GLY105 surround the ligand and reinforce the binding conformation. The detailed receptor-ligand interactions of compound **5c** with the four α-amylase targets are summarized in Table 6. The best docking poses of the ligand with the selected targets, showing the 3D and 2D visualizations of the receptor-ligand interactions, are presented in Fig. 12 and Fig. 13. Other derivatives such as **5d, 5e, 5 g, 5h**, and **5j** exhibited lower *in vitro*α-amylase inhibition, yet they displayed good docking scores ranging from -6.2 to -7.8 kcal mol^{-1}, thus opening new avenues for further research and highlighting the need for further investigation into their structural or pharmacokinetic properties. Overall, the binding of **5c** across multiple α-amylase targets is mediated by a combination of heterocyclic hydrogen bonding, π–π stacking, and hydrophobic contacts involving the oxadiazole, pyridine, and piperazine fragments, collectively explaining its superior docking profile and supporting its potential as a promising lead for the design of potent α-amylase inhibitors for antidiabetic therapy.

4.9. *In silicoADME analysis*

The druglikeliness and the ADME properties of the compound **5c** were calculated using the SwissADME tool. The contrasting results are compiled in Table 7. The molecule possesses favourable log p indicating the optimal value for oral drug. The compound has suitable number of hydrogen bond donors (HBD) and acceptors (HBA) according to Lipinsky's rule of five where the maximum number of HBD and HBA should be 5 and 10 respectively [47]. The table shows that the molecule has standard value for topological polar surface area (TPSA) with favourable polarity for oral absorption. High value of TPSA leads to poor membrane permeability and less gastrointestinal absorption [67]. There are zero violations of both lead likeliness and drug likeliness criteria reflecting its suitability as an orally bioavailable therapeutic agent. The synthetic accessibility of the compound is found to be 3.05. The bioavailability radar (Fig. 14a) suggests that the compound falls within the optimal range of physicochemical space for the parameters considered in the study supporting its oral drug-likeliness. Further, the boiled egg pose (Fig. 14b) positions the compound in the white region as a blue dot. This suggest that although the compound has high probability of gastro intestinal absorption, its ability for blood brain barrier penetration is limited because of its identification as P-glycoprotein substrate. Collectively, these results suggest that the compound is well suitable as a promising orally bioavailable drug candidate.

5. Conclusion

This study reports the synthesis and characterization of a novel series of pyridine-linked 1,3,4-oxadiazole derivatives (**5a–5j**), confirmed through detailed spectral analyses. Biological screening revealed that compound **5c** exhibited the strongest α-amylase inhibition ($IC_{50} = 106.1 \pm 1.21$ μM), acting via a non-competitive mechanism as confirmed by kinetic analysis. Molecular docking demonstrated that 5c forms multiple hydrogen bonds (2.4–3.6 Å), π–π stacking, and hydrophobic interactions within the α-amylase active site, yielding superior docking scores (-7.7 to -8.0 kcal mol^{-1}) compared with acarbose. DFT and MEP analyses supported its electronic stability and electrostatic complementarity, while in silico ADME profiling indicated favorable lipophilicity (log $P =$ 0.42), zero rule violations, good gastrointestinal absorption, and oral drug-likeness. Collectively, these experimental and theoretical findings identify compound **5c** as a promising lead scaffold for developing potent, orally bioavailable α-amylase inhibitors. Further *in vivo* validation and structural optimization are warranted to advance this framework toward next-generation antidiabetic therapeutics.

CRediT authorship contribution statement

Chandan Mallikarjuna: Writing – review & editing, Writing – original draft, Software, Methodology, Data curation, Conceptualization. **Udaya Kumar A. H:** Visualization, Validation, Software, Data curation. **Karthik Kumara:** Visualization, Validation, Software, Data curation. **Rekha N Dharmappa:** Visualization, Software, Data curation. **Dinesh Kumar G:** Validation, Data curation. **Neratur Krishnappagowda Lokanath:** Validation, Supervision, Methodology, Investigation, Conceptualization. **Kariyappa Ajay Kumar:** Writing – review & editing, Writing – original draft, Validation, Supervision, Methodology, Investigation.

Declaration of competing interest

The authors declare that they have no known competing financial interests or personal relationships that could have appeared to influence the work reported in this paper.

Acknowledgments

The authors are grateful to the National Single Crystal Diffractometer Facility, Department of Studies in Physics, University of Mysore, for the X-ray diffraction studies, and to the USIC, JSS Academy of Higher Education and Research (JSS University), for recording the spectra.

Supplementary materials

Supplementary material associated with this article can be found, in the online version, at doi:10.1016/j.molstruc.2025.144655.

Data availability

The data that has been used is confidential.

References

[1] M. Taha, N.H. Ismail, W. Jamil, S. Imran, F. Rahim, S.M. Kashif, M. Zulkefeli, Med. Chem. Res. 25 (2016) 225–234.
[2] Z.T. Bloomgarden, J. Diabetes. 12 (2020) 347–348.
[3] K. Balan, P. Ratha, G. Prakash, P. Viswanathamurthi, S. Adisakwattana, T. Palvannan, Arab. J. Chem. 10 (2017) 732–738.
[4] D. Kalita, D.G. Holm, D.V. LaBarbera, J.M. Petrash, S.S. Jayanty, PLoS. One 13 (2018) e0191025.
[5] A.K. Rines, K. Sharabi, C.D. Tavares, P. Puigserver, Nat. Rev. Drug Discov. 15 (2016) 786–804.
[6] S. Imran, M. Taha, M. Selvaraj, N.H. Ismail, S. Chigurupati, J.I. Mohammad, Bioorg. Chem. 73 (2017) 121–127.
[7] S. Ghosh, P. More, A. Derle, A.B. Patil, P. Markad, A. Asok, N. Kumbhar, M. L. Shaikh, B. Ramanamurthy, V.S. Shinde, PLoS. One 9 (2014) e106039.
[8] H. Wang, Y.J. Du, H.C. Song, Food Chem. 123 (2010) 6–13.
[9] (a) R.M. Jones, J.N. Leonard, D.J. Buzard, J. Lehmann, Expert. Opin. Ther. Pat. 19 (2009) 1339–1359;
(b) G. Anjanayya, R. Gani, A. Kudva, S. Joshi, M. Hiremath, A. Kavital, K. Timanagouda, B. Mathada, M. Javeed, R. Aziz, J. Iran Chem. Soc. 21 (2024) 2221–2237.
[10] H.-Z. Zhang, S. Kasibhatla, J. Kuemmerle, W. Kemnitzer, K. Ollis-Mason, L. Qiu, C. Crogan-Grundy, B. Tseng, J. Drewe, S.X. Cai, J. Med. Chem. 48 (2005) 5215–5223.
[11] M.F. Mohamed, E.A. Ahmed, O. Alshazly, O.A. Omran, R.A. Soomro, A. Nafady, J. Mol. Struct. 1331 (2025) 141651.
[12] D.M. Cottrell, J. Capers, M.M. Salem, K. DeLuca-Fradley, S.L. Croft, K. A. Werbovetz, Bioorg. Med. Chem. 12 (2004) 2815–2824.
[13] I. Kapila, A. Bharwal, P. Sharma, N. Choudhary, V. Abbot, Eur. J. Med. Chem. Rep. 11 (2024) 100150.
[14] M. Ono, M. Haratake, H. Saji, M. Nakayama, Bioorg. Med. Chem. 16 (2008) 6867–6872.
[15] B.S. Orlek, F.E. Blaney, F. Brown, M.S. Clark, M.S. Hadley, J. Hatcher, G.J. Riley, H. E. Rosenberg, H.J. Wadsworth, P. Wyman, J. Med. Chem. 34 (1991) 2726–2735.
[16] K. Goldberg, S. Groombridge, J. Hudson, A.G. Leach, P.A. MacFaul, A. Pickup, R. Poultney, J.S. Scott, P.H. Svensson, J. Sweeney, Medchemcomm. 3 (2012) 600–604.
[17] B. Bashir, W. Shahid, M. Ashraf, M. Saleem, S. Muzaffar, M. Imran, H. Amjad, K. Bhattarai, N. Riaz, Bioorg. Chem. 115 (2021) 105243.
[18] M.D. Formagio, J.V.D.O. Silva, A.F. Silva, P.A.Z. Campanerut-Sá, A. Urbano, P.D. S. Bonfim-Mendonça, I.R.G. Capoci, É.S.K. Cotica, J.M.G. Mikcha, Lett. Appl. Microbiol. 77 (2024) ovad138.
[19] A. Murmu, P. Banjare, B.W. Matore, P.P. Roy, J. Singh, Curr. Med. Chem. 31 (2024) 6227–6250.
[20] D.R. Faria, R.C. Melo, G.S. Arita, K.M. Sakita, F.A.V. Rodrigues-Vendramini, I.R. G. Capoci, T.C.A. Becker, P. d S Bonfim-Mendonça, M.S.S. Felipe, T.I.E. Svidzinski, Pathogens 10 (2021) 314.
[21] L.H. Al-Wahaibi, A.A. Mohamed, S.S. Tawfik, H.M. Hassan, A.A. El-Emam, Molecules. 26 (2021) 2110.
[22] V. Sharma, R. Das, D.K. Mehta, D. Sharma, Mol. Divers 29 (2025) 1911–1928.
[23] M.G. Srinivasa, J.G. Paithankar, S.R.S. Birangal, A. Pai, V. Pai, S.N. Deshpande, B. Revanasiddappa, RSC Adv. 13 (2023) 1567–1579.
[24] V.C. Basappa, S. Penubolu, D.K. Achutha, A.K. Kariyappa, J. Chem. Sci. 133 (2021) 55.
[25] S. Jisha, G. Nagesh, P. Karunakar, G. Nidhi, B. Sridhar, S. Basavarajaiah, J. Iran Chem. Soc. 22 (2025) 717–731.
[26] K.D. Patel, S.M. Prajapati, S.N. Panchal, H.D. Patel, Synth. Commun. 44 (2014) 1859–1875.
[27] K. Manjunatha, B. Poojary, P.L. Lobo, J. Fernandes, N.S. Kumari, Eur. J. Med. Chem. 45 (2010) 5225–5233.
[28] E. Barber, M.J. Houghton, G. Williamson, Foods. 10 (2021) 1939.
[29] N. Cele, P. Awolade, P. Seboletswe, K. Olofinsan, M.S. Islam, P. Singh, Pharmaceuticals 15 (2022) 1035.
[30] T. Hiyoshi, M. Fujiwara, Z. Yao, J. Biomed. Res. 33 (2017) 1.
[31] Y. Hamada, Pyridine (2018) 9–26.
[32] G.R. Jadhav, D.G. Deshmukh, V.J. Medhane, V.B. Gaikwad, A.D. Bholay, Heterocycl. Comm. 22 (2016) 123–130.
[33] P. Patil, S. Sethy, T. Sameena, K. Shailaja, Asian J. Res. Chem. 6 (2013) 888–899.
[34] D. Dua, P. Kumar, R. Anand, S. Sood, G. Singh, Med. Chem..
[35] S. De, A.K. SK, S.K. Shah, S. Kazi, N. Sarkar, S. Banerjee, S. Dey, RSC. Adv. 12 (2022) 15385–15406.
[36] M.D. Jalageri, A. Nagaraja, Y.M. Puttaiahgowda, RSC. Adv. 11 (2021) 15213–15230.
[37] A.P. Kourounakis, D. Xanthopoulos, A. Tzara, Med. Res. Rev. 40 (2020) 709–752.
[38] S. Asirvatham, E. Thakor, H. Jain, T. Morpholine, J Chem Rev (2021) 3.
[39] N.A. Frolov, A.N. Vereshchagin, Int. J. Mol. Sci. 24 (2023) 2937.
[40] H. Ullah, I. Uddin, H.Z. Ali, W. Hassan, G. Mehnaz, L. Maryam, M. Sarfraz, M. S. Khan, M.S. Islam, Z.M. Almarhoon, Results. Chem. 11 (2024) 101832.
[41] N. Hosseini Nasab, H. Raza, Y.S. Eom, F.H. Shah, J.-H. Kwak, S.J. Kim, Mol. Divers. 29 (2025) 43–59.
[42] R. Nithyabalaji, H. Krishnan, J. Subha, R. Sribalan, J. Mol. Struct. 1204 (2020) 127563.
[43] S.S. Hamdani, B.A. Khan, M.N. Ahmed, S. Hameed, K. Akhter, K. Ayub, T. Mahmood, J. Mol. Struct. 1200 (2020) 127085.
[44] M. Nawaz, M. Taha, F. Qureshi, N. Ullah, M. Selvaraj, S. Shahzad, S. Chigurupati, A. Waheed, F.A. Almutairi, BMC. Chem. 14 (2020) 43.
[45] S.B. Kalli, V. Velmurugan, Pharmacia 69 (2022) 987–993.
[46] C.H. Jhong, J. Riyaphan, S.H. Lin, Y.C. Chia, C.F. Weng, Biofactors 41 (2015) 242–251.
[47] C.A. Lipinski, F. Lombardo, B.W. Dominy, P.J. Feeney, Adv. Drug Deliv. Rev. 23 (1997) 3–25.
[48] K. Kumara, A.D. Kumar, S. Naveen, K.A. Kumar, N. Lokanath, J. Mol. Struct. 1161 (2018) 285–298.
[49] G.M. Sheldrick, Acta Crystallogr. A Found Adv. 71 (2015) 3–8.
[50] (a) G.M. Sheldrick, T.R. Schneider, Methods in Enzymology, 277, Elsevier, 1997, pp. 319–343. *Vol*;
(b) O.V. Dolomanov, L.J. Bourhis, R.J. Gildea, J.A. Howard, H. Puschmann, J. Appl. Crystallogr. 42 (2009) 339–341.
[51] O.V. Dolomanov, L.J. Bourhis, R.J. Gildea, J.A. Howard, H. Puschmann, Appl. Crystallogr. 42 (2009) 339–341.
[52] A. Spek, Found Crystallogr. 46 (1990) c34, c34.
[53] C.F. Macrae, P.R. Edgington, P. McCabe, E. Pidcock, G.P. Shields, R. Taylor, M. Towler, J. Streek, Appl. Crystallogr. 39 (2006) 453–457.
[54] C.F. Mackenzie, P.R. Spackman, D. Jayatilaka, M.A. Spackman, IUCrJ. 4 (2017) 575–587.
[55] U.K.A.H Mahesha, P.K.J N.V. Harohally, C. Krishnamurthy, K. Jathi, A. Ahmad, M. B. Alshammari, N.K. Lokanath, ACS Omega 9 (2024) 30109–30119.
[56] I.Y. Zhang, J. Wu, X. Xu, Chem. Commun. 46 (2010) 3057–3070.
[57] T. Yanai, D.P. Tew, N.C. Handy, Chem. Phys. Lett. 393 (2004) 51–57.
[58] M. Robb, Expand limits Comput. Chem. (2022). https://gaussian.com/g16new.
[59] A.H. Udaya Kumar, K. Kumara, N.V. Harohally, K.J. Pampa, N.K. Lokanath, ChemistrySelect. 6 (2021) 6240–6255.
[60] H. Phetmung, K. Musikapong, T. Srichana, J. Therm. Anal. Calorim. 138 (2019) 1207–1220.
[61] O. Trott, A.J. Olson, J. Comput. Chem. 31 (2010) 455–461.
[62] D. Studio, Accelrys 420 (2008) 1–9.
[63] L. Yurttaş, A.E. Evren, A. Kubilay, M.O. Aksoy, H.E. Temel, G. L E Akalın Çiftçi, ACS Omega 8 (2023) 49311–49326.
[64] A. Daina, O. Michielin, V. Zoete, Sci. Rep. 7 (2017) 42717.
[65] M.G. Acker, D.S. Auld, Perspect. Sci. 1 (2014) 56–73.
[66] F. Azimi, J.B. Ghasemi, H. Azizian, M. Najafi, M.A. Faramarzi, L. Saghaei, H. Sadeghi-Aliabadi, B. Larijani, F. Hassanzadeh, M. Mahdavi, Int. J. Biol. Macromol. 166 (2021) 1082–1095.
[67] J.D. Hughes, J. Blagg, D.A. Price, S. Bailey, G.A. DeCrescenzo, R.V. Devraj, E. Ellsworth, Y.M. Fobian, M.E. Gibbs, R.W. Gilles, Bioorg. Med. Chem. Lett. 18 (2008) 4872–4875.